PNAS
www.pnas.org

Supplementary Information for

Kinetic analysis of the multi-step aggregation pathway of human transthyretin

Xun Sun, H. Jane Dyson, Peter E. Wright*

Correspondence to Peter E. Wright
Email: wright@scripps.edu

This PDF file includes:

Supplementary text
Figs. S1 to S9
References for SI reference citations

www.pnas.org/cgi/doi/10.1073/pnas.1807024115

Supplementary Information Text

Protein Expression, Purification and Labeling. All constructs were based on a pET29a plasmid encoding the human WT TTR sequence with an N-terminal methionine. Site-directed mutagenesis was performed using the QuikChange kit (Agilent). Primer sequences for designated mutations are:

S85C:
5'-catggaatgggcagatgccaagtgccttcca-3'; 5'-tggaaggcacttggcatctgcccattccatg-3'.
V30M:
5'-ctttctgaacacatgcatggccacattgatggcag-3';5'-ctgccatcaatgtggccatgcatgtgttcagaaag-3'.
L55P:
5'-gttgtgagcccatgcggctctccagactcac-3';5'-gtgagtctggagagccgcatgggctcacaac-3'.
F87A:
5'-tctgcatgctcatgggctgggcagatgccaagtgc-3';5'-gcacttggcatctgcccagcccatgagcatgcaga-3'.
T119M:
5'-gtgacgacagccatggtggaataggagtaggg-3';5'-ccctactcctattccaccatggctgtcgtcac-3'.
V122I:
5'-cttgggattggtgatgacagccgtggtgg-3';5'-ccaccacggctgtcatcaccaatcccaag-3'.

The proteins were expressed according to Ref (1). For all S85C-bearing constructs, the oxidized oligomers formed during expression were first purified using Sephacryl S200 and then passed through a Capto Q ImpRes column (GE Healthcare Life Sciences) as described previously (1). The oligomer fractions eluted with a solution conductance from 36 to 42 mS/cm were then reduced using 10 mM tris(2-carboxyethyl)phosphine (TCEP) for at least 1 hr at 298 K and re-loaded to the Capto Q ImpRes column to further separate the reduced TTR tetramer from high molecular weight impurities. The final fractions with a conductance around 26-29 mS/cm were collected. The TTR concentration was calculated as monomer concentration using an extinction coefficient of 18450 $M^{-1}cm^{-1}$.

For 3-bromo-1,1,1-trifluoroacetone (BTFA) labeling, reduced TTR mutants (100-500 μM) were incubated with 2 mM BTFA (Sigma) in 10 mM potassium phosphate and 100 mM KCl at pH 7.0 (GF buffer) for 1 hr at 298 K. The excess BTFA was then removed using a PD25 column (GE Healthcare Life Sciences). Electrospray ionization mass spectrometry confirmed that no unlabeled species remained. The molecular mass measured (14002.0 Da) agreed well with the calculated mass for C10S-S85C-BTFA TTR (TTR^F, 14002.6 Da).

Kinetics Analysis. Since the aggregates (A) in Scheme 1 (see main text) are likely to be a mixture of heterogeneous oligomers, protofibrils and mature fibrils (2), it was not possible to use an explicit stoichiometry of TTR protomers to specify the kinetic order for the oligomerization rate constant k_2 in a standard manner. As a simplified approach, a set of first-order kinetics equations was used instead. The first-order ordinary differential equations (ODEs) for Scheme 1 are:

$$\frac{d[T]}{dt} = -k_1[T] + k_{-1}[I]$$
$$\frac{d[I]}{dt} = -(k_2 + k_{-1})[I] + k_1[T] + k_{-2}[A] \quad \textbf{[S1]}$$
$$\frac{d[A]}{dt} = -k_{-2}[A] + k_2[I]$$

where […] denotes concentrations of the designated species and k_x represents the pseudo first-order kinetic rates. The T, I and A states represent the TTR protomer in the forms of tetramer, intermediate(s), and NMR-invisible aggregates, respectively. The similar ^{19}F T_1 values of T (0.33 ± 0.03 s) and I (0.39 ± 0.06 s) at pH 4.4 and 298 K eliminated the need for T_1 correction in quantification of the populations. Consequently, integrated ^{19}F peak areas of T and I were used directly to quantitate the relative population of the CF_3 probes on the TTR protomer in these two states. The total amount of TTR was determined from the combined peak areas of T and I at the first data point acquired after lowering the pH to 4.4. The missing amplitude (A signal) was determined by subtracting both the T and I peak areas from the total TTR amount to ensure mass conservation, as required by Scheme 1 and Eq. **S1**. We further normalized [*T*], [*I*] and [*A*] using the total TTR amount such that [*T*] + [*I*] + [*A*] = 100%. The summed squared residuals between these time-dependent experimental data and trial ODEs solved by the numerical ODE solver (*ode23*) were minimized using the nonlinear curve fitting function *lsqcurvefit* with trust-region-reflective as the minimizing algorithm (MATLAB). We also tested another minimizer *fminsearch* that gave very similar fitting results. Uncertainty was estimated as one standard deviation from 50 bootstrap datasets. The reported fitting uncertainties are greater than or similar to the rate differences from independently repeated experiments.

Applying a boundary condition where the initial relative concentration is 100% for T ($[T]_0$ = 100%, $[I]_0$ = 0 and $[A]_0$ = 0), the time-dependent analytical expressions of T, I and A are (3):

$$[T(t)] = [T]_0\left(\frac{k_{-1}k_{-2}}{\gamma_1\gamma_2} - \frac{k_1(\gamma_1 - k_2 - k_{-2})}{\gamma_1(\gamma_2 - \gamma_1)}e^{-\gamma_1 t} - \frac{k_1(k_2 + k_{-2} - \gamma_2)}{\gamma_2(\gamma_2 - \gamma_1)}e^{-\gamma_2 t}\right)$$
$$[I(t)] = [T]_0 k_1\left(\frac{k_{-2}}{\gamma_1\gamma_2} - \frac{k_{-2} - \gamma_1}{\gamma_1(\gamma_2 - \gamma_1)}e^{-\gamma_1 t} + \frac{k_{-2} - \gamma_2}{\gamma_2(\gamma_2 - \gamma_1)}e^{-\gamma_2 t}\right) \quad \textbf{[S2]}$$
$$[A(t)] = [T]_0 k_1 k_2\left(\frac{1}{\gamma_1\gamma_2} - \frac{1}{\gamma_1(\gamma_2 - \gamma_1)}e^{-\gamma_1 t} + \frac{1}{\gamma_2(\gamma_2 - \gamma_1)}e^{-\gamma_2 t}\right)$$

where the two exponential terms are the relaxation/decay rates in Scheme 1:

$$\gamma_1 = \left(b + \sqrt{b^2 - 4a}\right)/2$$
$$\gamma_2 = \left(b - \sqrt{b^2 - 4a}\right)/2 \quad \textbf{[S3]}$$

where $a = k_1k_2 + k_1k_{-2} + k_{-1}k_{-2}$ and $b = k_1 + k_2 + k_{-1} + k_{-2}$. Since all rates are greater than zero, it is straightforward to prove that $b^2 - 4a > 0$ and that both relaxation rates are real numbers. Although Scheme 1 was modeled numerically for the consideration of robustness, these analytical equations offer mechanistic insights into the temperature-dependent kinetic

parameters, including rates of all four elementary steps, two relaxation rates and their relative amplitudes (see below).

Loss of amplitude of the T signal is described by two exponential decays (fast γ_1 and slow γ_2). The amplitude (*Amp*) ratio of slow decay γ_2 and fast decay γ_1 is:

$$\frac{Amp_{\text{slow}}}{Amp_{\text{fast}}} = \frac{\gamma_1}{\gamma_2} \times \frac{\left(k_2 + k_{-2} - \gamma_2\right)}{\left(\gamma_1 - k_2 - k_{-2}\right)} \qquad \textbf{[S4]}$$

Although there are four different terms involved in Eq. **S4**, the most crucial term to render a smaller ratio at lower temperature is k_2+k_{-2}-γ_2, given the experimental rates for TTR^F, $F87A^F$ and $V122I^F$ (Table 1). Taking TTR^F as an example, the term of k_2+k_{-2}-γ_2 is 0.70 hr^{-1} at 310 K and reduces to 0.01 hr^{-1} at 277 K (ca. 70-fold). As a result, the slow/fast amplitude ratio in Eq. **S4** decreases from 24 at 310 K to 0.28 at 277 K (ca. 85-fold, also see Fig. S6*A* for similar trends for other two mutants).

To obtain further kinetic insights into the reduced k_2+k_{-2}-γ_2 term in the T signal of TTR^F at 277 K, it is useful to replace γ_2 (Eq. **S4**) with a simpler expression. To do so, we define $\Omega = k_1+k_{-1}-k_2-k_{-2}$ (> 0 based on TTR rates in Table 1). Then the term k_2+k_{-2}-γ_2 can be regrouped according to:

$$k_2 + k_{-2} - \gamma_2 = \frac{\sqrt{b^2 - 4a} - \Omega}{2} = \frac{\sqrt{\Omega^2 + 4k_{-1}k_2} - \Omega}{2} \approx \frac{k_{-1}k_2}{\Omega} \qquad \textbf{[S5]}$$

where the approximation step is done by expanding a Taylor series to the first order. Now it is clear that the reduction in k_2+k_{-2}-γ_2 is linked to the forward oligomerization rate k_2 and monomer tetramerization rate k_{-1} and Ω. The former two rates decrease substantially at 277 K as compared to 310 K (Table 1). For the denominator, Ω, the reduction in k_{-1} (0.60 hr^{-1}) is outweighed by the decrease in k_2 (0.70 hr^{-1}) from 277 K to 310 K. In addition, the tetramer dissociation rate k_1 is increased at 277 K compared to 310 K. Therefore, Ω is greater at 277 K (0.45 hr^{-1}) than 310 K (0.09 hr^{-1}). Taken together, the decreased term k_2+k_{-2}-γ_2 in TTR^F at 277 K is largely responsible for the reduced relative amplitude of the slow decay (Eq. **S4**). Analogous results were found for $F87A^F$ (k_2+k_{-2}-γ_2 from 0.08 hr^{-1} at 310 K to 0.01 hr^{-1} at 277 K) and $V122I^F$ (k_2+k_{-2}-γ_2 from 0.72 hr^{-1} at 310 K to 0.002 hr^{-1} at 277 K).

The steady state population of the I signal is enhanced at low temperature. The relative steady state populations of the T, I and A states (T_{steady}, I_{steady} and A_{steady}) are given by:

$$\begin{aligned} T_{\text{steady}} &= k_{-1}k_{-2} / a \\ I_{\text{steady}} &= k_1 k_{-2} / a \\ A_{\text{steady}} &= k_1 k_2 / a \end{aligned} \qquad \textbf{[S6]}$$

Calculated values of I_{steady} were used in generating Fig. 5*B* based on fitted rates (Table 1).

The time at which the I signal reaches the maximum (t_{max}) also provides kinetic insights. Setting $d[I(t)]/dt = 0$, we arrive at:

$$t_{\text{max}} = \frac{1}{\gamma_1 - \gamma_2} \log\left(\frac{\gamma_1 - k_{-2}}{\gamma_2 - k_{-2}}\right) \qquad \textbf{[S7]}$$

where the reduced γ_1-γ_2 term contributes more critically to the increased t_{max} at low temperature (Fig. S6*B*) than the logarithm term (Table 1).

To obtain further insight into the kinetic contributions of the four rates to γ_1-γ_2 in Eq. **S7**, we show the following inequalities:

$$\min\{k_i\} < \gamma_2 < k_2 + k_{-2} < k_1 + k_{-1} < \gamma_1 < \sum_i k_i \qquad \textbf{[S8]}$$

where the central inequality between k_2+k_{-2} and k_1+k_{-1} is based on the measured TTR rates (Table 1) and the other inequalities always hold as long as all four rates are positive. Based on Eq. **S8**, for TTR^F and $V122I^F$, the greatly reduced forward oligomerization rate k_2 and monomer tetramerization rate k_{-1} at low temperature outnumber the gain by tetramer dissociation rate k_1 so the rate sum is reduced at low temperature (1.61 hr^{-1} to 0.55 hr^{-1} from 310 K to 277 K for TTR^F, 3.74 hr^{-1} to 1.15 hr^{-1} for $V122I^F$). This puts a smaller upper bound on γ_1, which is the main reason for a reduced γ_1-γ_2 at low temperature (also considering that the absolute change of γ_1 is more than that of γ_2, Table 1). In the case of $F87A^F$, k_1 also reduces at low temperature, which further contributes a smaller γ_1-γ_2 (Table 1).

The slower relaxation rate, γ_2 denotes the rate of increase in the missing signal amplitude ([$A(t)$] in Eq. **S2**). This rate at 310 K was compared with the single exponential OD approximation at the same temperature due to the relatively small lag time (<1 hr) between these two signals with respect to the overall aggregation process (~ 2 d). Numerical simulations showed a small ~5% error between the exact analytic solution of the slow relaxation rate (γ_2 in Eq. **S3**) and the single exponential estimate for the NMR A signal simulated using the TTR^F experimental parameters at 310 K. This numerical simulation justified the NMR and OD kinetics comparison at this temperature (Fig. S5*C*). Due to the increased lag time between the NMR A signal and OD data at 298 K and 277 K, we used $t_{1/2}$ (the time to reach 50% maximal signal) to compare these two signals (Fig. S6*C*), where $t_{1/2}$ for OD is longer than that measured by NMR due to a reduced forward fibrillization/aggregation rate at low temperature (Fig. S7).

The apparent activation energies were estimated by transition state theory assuming that the transmission coefficient is unity:

$$\Delta G^{\dagger} = RT\left[\log\left(k_B T/h\right) - \log\left(k\right)\right] \qquad \textbf{[S9]}$$

where k is the measured rate, R is the gas constant, T is temperature, k_B is the Boltzmann constant and h is the Planck constant. The common factor of $RT\log(k_BT/h)$ is subtracted from the apparent activation energy to facilitate comparison of the energetic differences at each temperature (Fig. 6). Using experimentally measured rates, the apparent equilibrium constants ($K_{app,1}$= k_1/k_{-1} and $K_{app,2}$= k_2/k_{-2}) (Figs. 5*C-D*) and apparent Gibbs free energy changes (ΔG_{app}=-$RT\log(K_{app})$) were also calculated (Fig. 6).

Similar first-order kinetics approximations have been reported for multi-step enzymatic reactions (4, 5). It is likely that many elementary steps may be involved when aggregates are formed by self-association of intermediates. While alternative models with additional steps and kinetic species are certainly possible (for example, two sequential intermediates in one kinetics scheme between the T and A species, $T \rightleftharpoons I_1 \rightleftharpoons I_2 \rightleftharpoons A$, I_1 for monomer,

and I_2 for low molecular weight intermediates as the observed broad peaks for TTR^F at 277 K in Fig. S4*A*), Scheme 1 is a maximum parsimony model, where these aggregation kinetic steps are condensed into one single reversible step with two rates (k_2 and k_{-2}). See Table 1 for TTR variants that show intermediates with quantifiable intensities (TTR^F, $F87A^F$ and $V122I^F$ at 277 K, 298 K and 310 K, and $L55P^F$ at 277 K).

For TTR variants that did not form observable intermediates, a single exponential ($V30M^F$ at 310 K and 298 K) or double exponential function ($V30M^F$ at 277 K, $L55P^F$ at 298 K and 310 K) was used to fit the tetramer decay kinetics (Fig. S9). For $L55P^F$, a double exponential function (adjusted $R^2 = 0.998$ at 298 K and 0.996 at 310 K, respectively) fits better than a single exponential fit at both temperatures (adjusted $R^2 = 0.981$ at 298 K, 0.982 at 310 K, respectively). The same is true for the $V30M^F$ tetramer decay at 277 K (adjusted $R^2 = 0.990$ for double exponential fit and 0.951 for single exponential fit). All fitting results are listed in Table 1.

Molecular Modeling. The molecular structure of BTFA coupled to L-Cys (Cys-BTFA) was optimized in Gaussian 09 A.02 at the level of HF/6-31G theory (6). The charge parameterization of geometrically optimized Cys-BTFA was computed using the AM1-BCC model (7). A tetramer model of TTR^F based on PDB 1BMZ (8) was prepared in AMBER 16 (9) with ff14SB as the force field (10). In this model, all four S85 residues were replaced with the optimized Cys-BTFA. The energy minimization was performed as previously reported (1). The final model is shown in Fig. 1, which was generated using PyMOL (11).

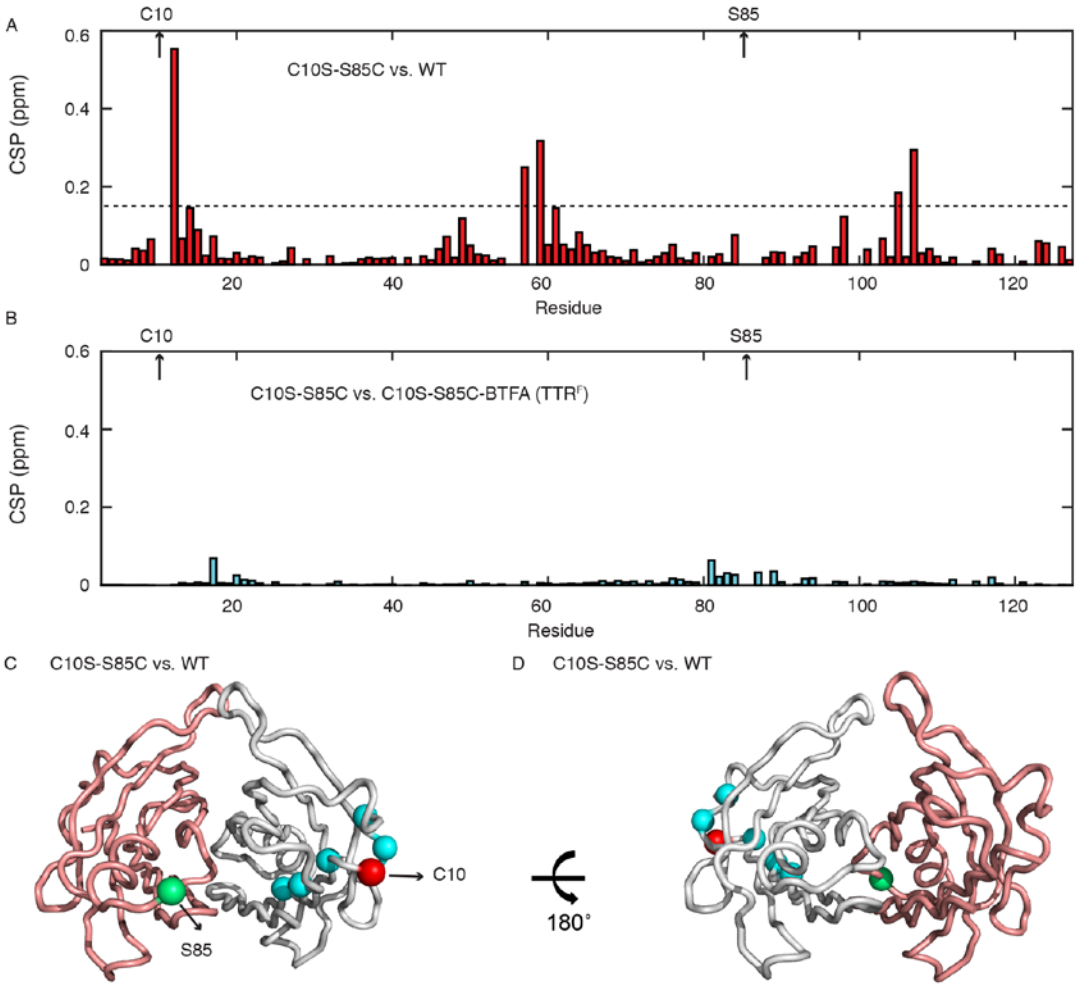

Fig. S1. Mapping backbone amide chemical shift perturbation (CSP) using ^{1}H-^{15}N HSQC spectroscopy. (*A*–*B*) Weighted average [^{1}H, ^{15}N] backbone amide CSP for C10S-S85/WT (*A*) and C10S-S85C/TTR^{F} (*B*) in GF buffer at pH 7.0 and 298 K. Both mutated residues are labeled on the top. The dashed line denotes two standard deviations in (*A*). All of the perturbed residues are localized close to C10. (*B*) The labeling of BTFA leads to only very small CSPs (< 0.1 ppm) localized around S85. (*C*–*D*) CSP from (*A*) mapped onto a dimeric model TTR structure (chains A and B from PBD: 1BMZ). The two chains are colored gray and coral. Cα locations of C10 in the gray chain and S85 in the coral chain are shown in red and green spheres, respectively. Residues with weighted average [^{1}H, ^{15}N] CSP larger than two standard deviations are colored in cyan for Cα in the gray chain. The weighted average backbone amide CSP was calculated using $\sqrt{\left(\Delta^{1}\mathrm{H}\right)^{2}+\left(\Delta^{15}\mathrm{N}/5\right)^{2}}$.

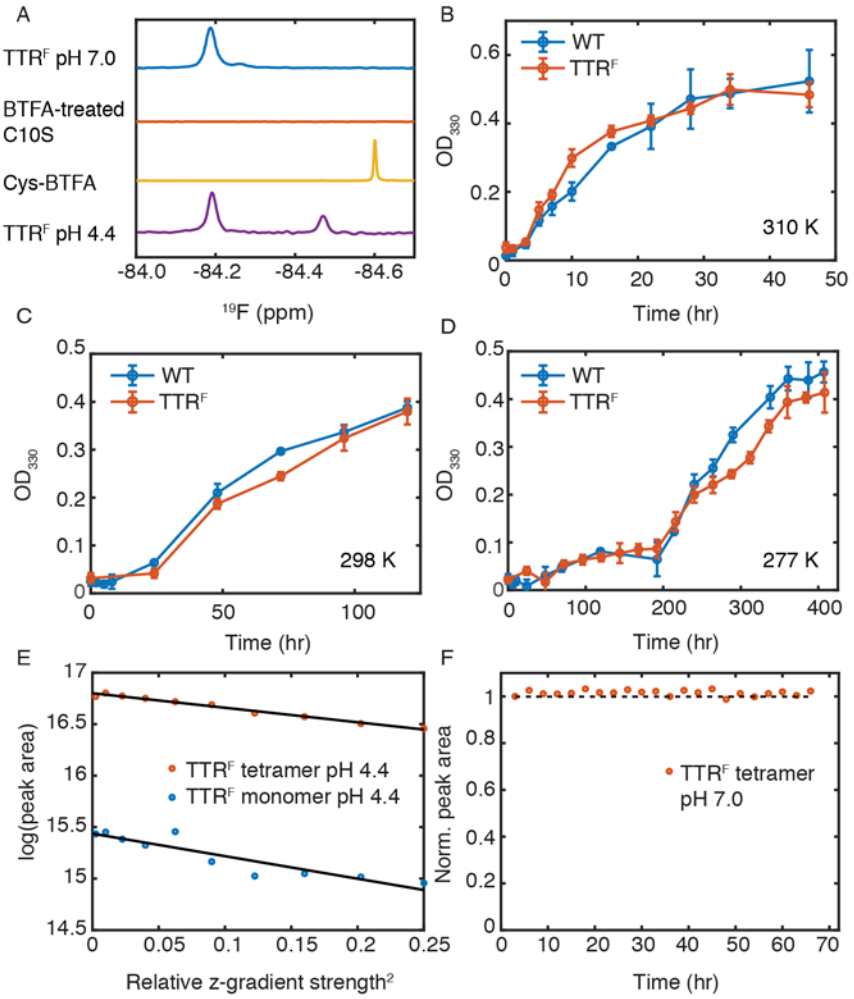

Fig. S2. Control experiments of TTR^F. (*A*) Comparison of ^{19}F-NMR spectra at 298 K. Unless otherwise mentioned, GF buffer at pH 7.0 is used. TTR^F at pH 7.0 is in blue. C10S treated with BTFA the same way as TTR^F is in red. Free Cys treated with BTFA is in orange. TTR^F in aggregation buffer at pH 4.4 and 298 K after 5 days is in purple. (*B–D*) Time-dependent changes in optical density at 330 nm (OD_{330}) for TTR^F and WT at 310 K (*B*), 298 K (*C*) and 277 K (*D*). Error bars represent one standard deviation from three independent measurements. Solid connecting lines are for eye guidance. (*E*) ^{19}F diffusion-ordered NMR experiment (DOSY). Plot of log(peak area) as a function of the square of the relative z-gradient strength. These data show that the ratio between the translational diffusion coefficients of monomer and tetramer is 1.55, in agreement with the prediction (1.53) based on the Stokes-Einstein equation and the estimated hydrodynamic radius (Eqs. **1–2**). Black solid lines are linear fits to the logarithms of peak areas of TTR^F tetramer (red) and monomeric intermediate (blue) against the squares of relative z-gradient strengths. (*F*) The tetramer peak area of TTR^F is constant at 298 K in GF buffer for at least 66 hr. Peak area is normalized to the first data point. The dashed line denotes a 100% of peak area with respect to the reference point.

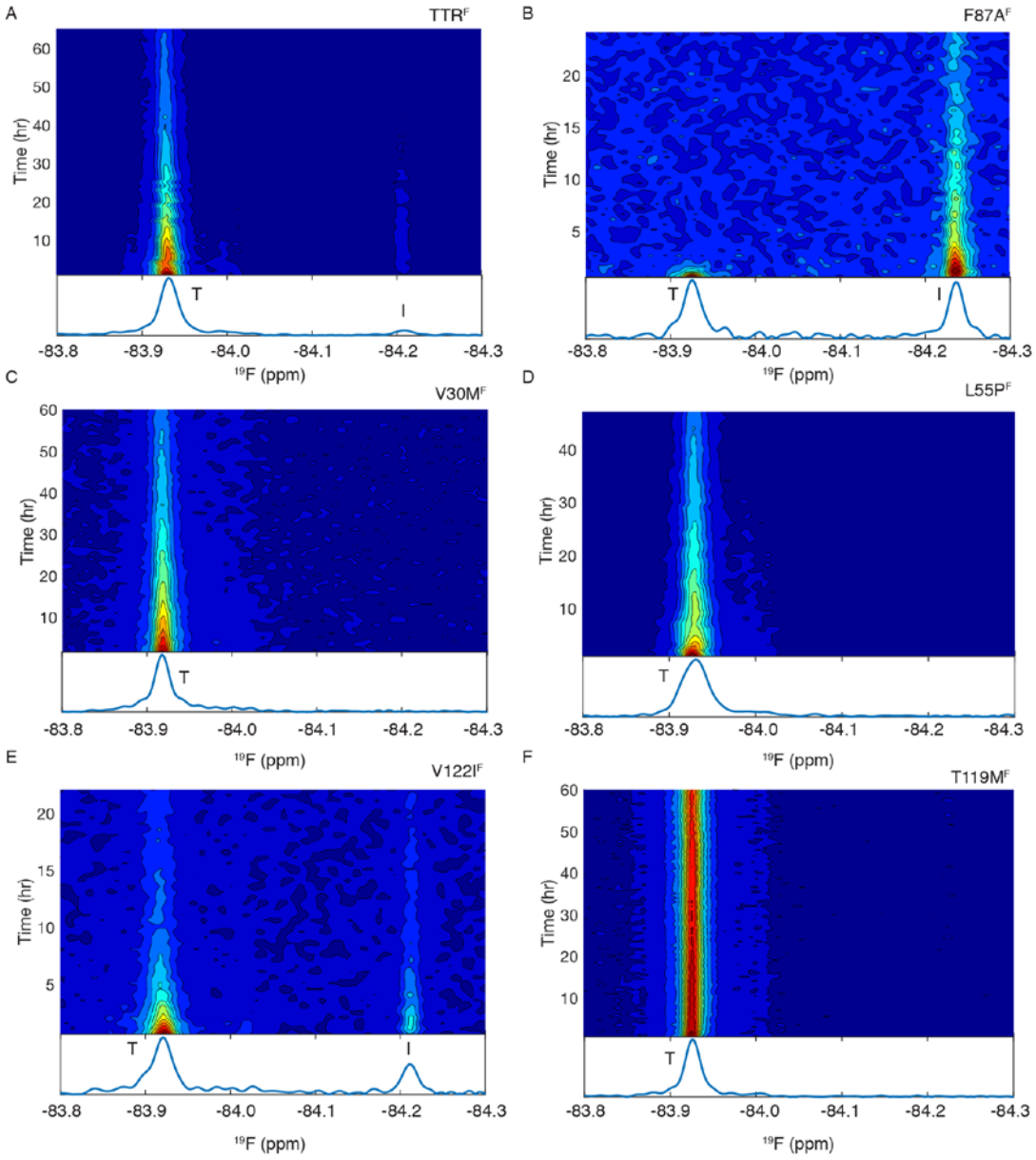

Fig. S3. Contour plots showing time dependence of ^{19}F-NMR signal intensity during aggregation at 310 K. The constructs are TTR^F (*A*), F87A^F (*B*), V30M^F (*C*), L55P^F (*D*), V122I^F (*E*) and T119M^F (*F*). The pH is adjusted to 4.4 from 7.0 at time zero. Relative intensity from high to low is colored from red to blue. A representative spectrum recorded from the 4th to 5th hour is shown below the contour for each construct except for F87A^F (*B*), where the spectrum of the 1st hour is shown since the decay of tetramer peak is rapid.

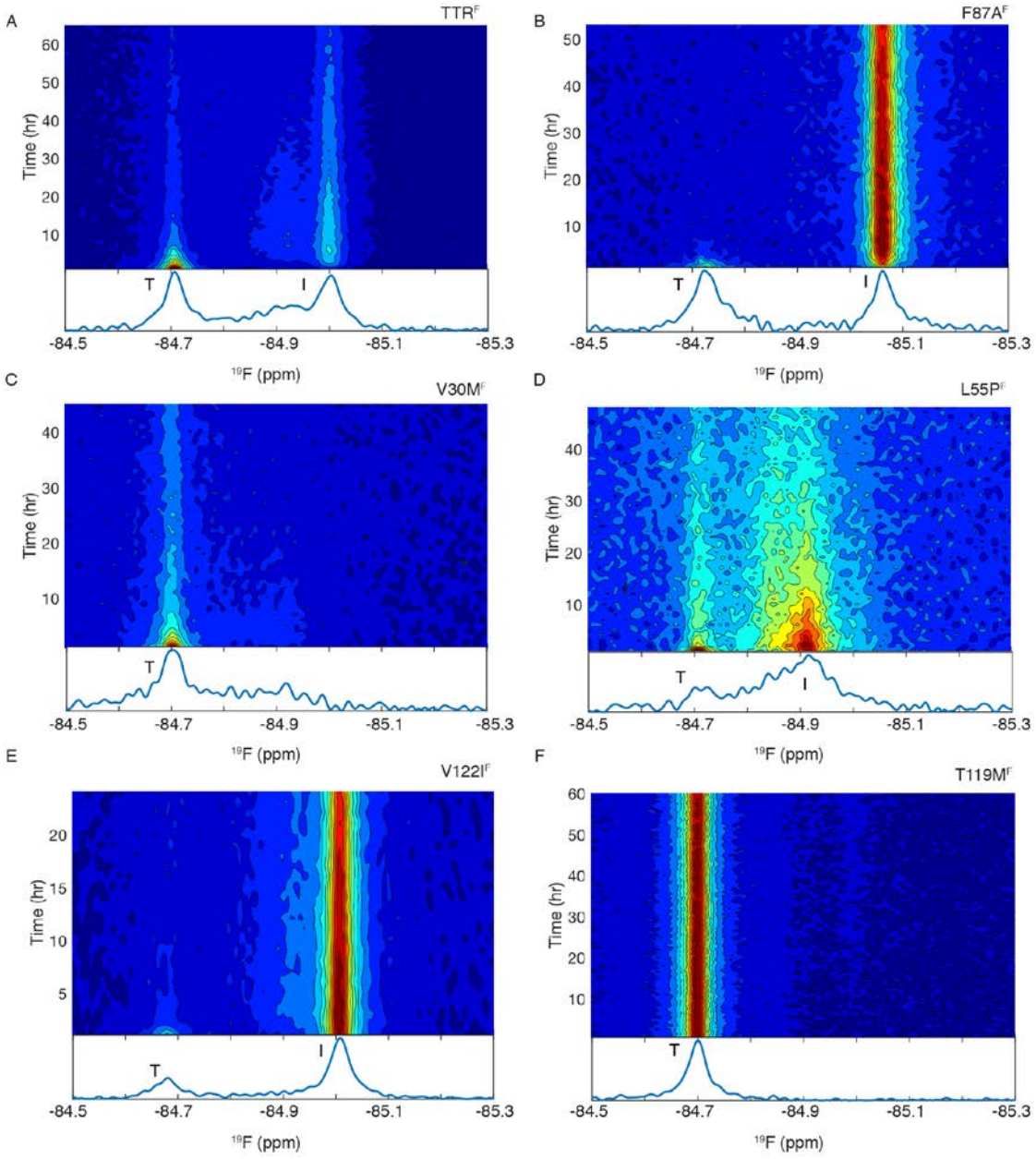

Fig. S4. Contour plots showing time dependence of ^{19}F-NMR signal intensity during aggregation at 277 K. The constructs are TTR^F (*A*), F87A^F (*B*), V30M^F (*C*), L55P^F (*D*), V122I^F (*E*) and T119M^F (*F*). The pH is adjusted from 7.0 to 4.4 at time zero. Relative intensity from high to low is colored from red to blue. A representative spectrum recorded from the 4th to 5th hour is shown below the contour for each construct except for F87A^F (*B*) and V122I^F (*E*), where the spectra of the 1st hour are shown since the decay of tetramer peak is rapid. Note broad peaks in V30M^F from ca. -84.8 to -85.0 ppm with low intensities as compared to the tetramer peak at -84.7 ppm (0–10 hr in *C*); due to low S/N, only the tetramer peak of V30M is used in fitting (Table 1). Similar broad peaks between tetramer and monomeric intermediate also appear in TTR^F (*A*), L55P^F (*D*) and, to a less extent, in V122I^F (*E*).

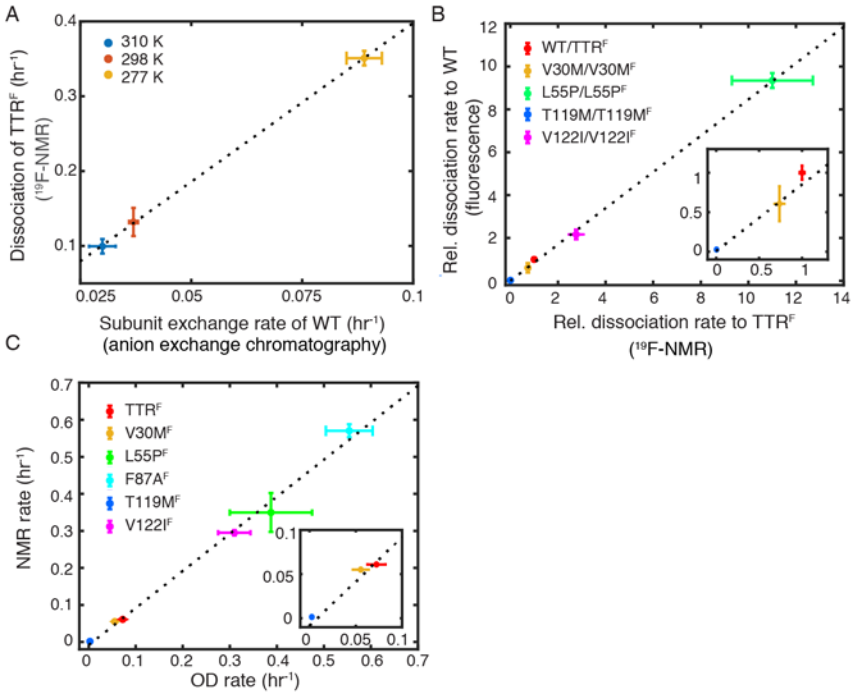

Fig. S5. Correlation between published data and rates measured by ^{19}F-NMR. (*A*) Correlation between tetramer dissociation rates of 10 μM TTR^F at pH 4.4 measured by ^{19}F-NMR (k_1) and the reported subunit exchange rates of WT at neutral pH (12, 13), where the monomer concentration was 14 μM at pH 7.4 for 310 K and 277 K and 20 μM at pH 7.6 for 298 K. The dashed line denotes the linear regression analysis with R^2 = 0.999 and a slope of 4.2. (*B*) Correlation of relative tetramer dissociation rates measured by ^{19}F-NMR (TTR^F as reference) and by fluorescence (WT as reference) (14). Inset: close-up to show data points for TTR^F, V30M^F and T119M^F. In Ref (14), urea-unfolding rates based on a two-state single exponential fitting at pH 7.0 and 298 K were extrapolated to afford the tetramer dissociation rates at 0 M urea. The ^{19}F-NMR tetramer dissociation rates at pH 4.4 and 277 K are used in comparison to minimize the complication of aggregation due to the coupled equilibria between dissociation and aggregation. The tetramer dissociation rates (k_1) in Scheme 1 for TTR^F, L55P^F and V122I^F are plotted. For the sake of comparison, single exponential fits of the tetramer decay signals for V30M^F and T119M^F are used as approximation since the same fitting was used in Ref (14). The correlation R^2 = 0.999 is obtained by linear regression analysis (dashed line). (*C*) Correlation between the rates at which the NMR A signal and the turbidity (OD_{330}) increase at 310 K. At this temperature, the rate of formation of higher order aggregates (detected by OD_{330}) is sufficiently high to rapidly deplete the small soluble oligomers that are visible by ^{19}F NMR. Inset: close-up to show data points for TTR^F, V30M^F and T119M^F. R^2 = 0.992 and the slope = 1.00 are obtained by linear regression (dashed line). For samples with observable intermediates (TTR^F, F87A^F and V122I^F), the rate of increase in the A signal is described by γ_2 in Eq. **S3**. For V30M^F and T119M^F, this rate is estimated by a single exponential fit of the tetramer signal decay. For L55P^F, the NMR rate corresponds to the faster decay rate in the double exponential fit of the tetramer signal. For OD rates, single exponential fits are used except for L55P^F, where the fast OD rate in the double exponential fit is compared to its faster NMR decay rate.

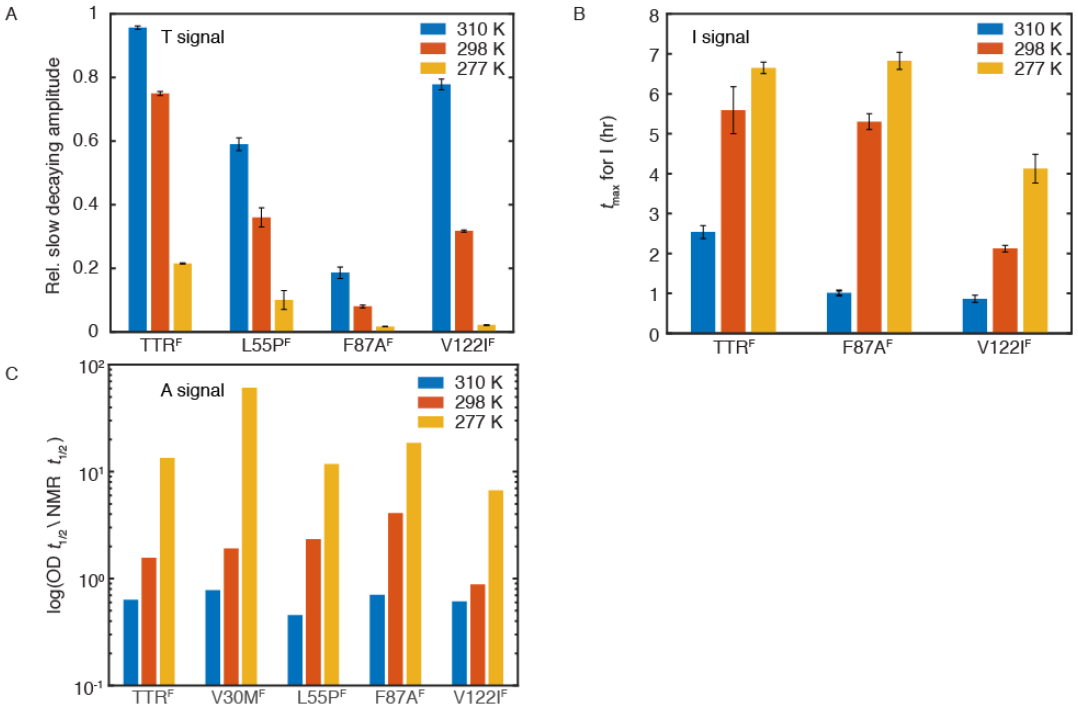

Fig. S6. Temperature-dependent kinetic parameters characterizing the NMR signals of the T (*A*), I (*B*) and A species (*C*) as a function of mutation. (*A*) The normalized slow decay amplitude in the tetramer peak decay. (*B*) The time for the maximal I signal (t_{max}). (*C*) The ratio of $t_{1/2}$ in OD_{330} over $t_{1/2}$ in the NMR A signal. (*A*) Decreasing temperature decreases the relative amplitude of the slow decay in the tetramer peak. The slow decay amplitudes of TTR^F, $F87A^F$ and $V122I^F$ are based on Eq. **S4**. The relative amplitudes of $L55P^F$ are from the tetramer signal fits due to the lack of intermediate at 298 K or higher (Fig. S9*E*-*F*). $V30M^F$ is not shown since the single exponential function fits its data at 310 K and 298 K reasonably well, suggesting a very minor amplitude (<5%) of the fast component, if any at all (Fig. S9*B*-*C*). Its data at 277 K are better fitted by a double exponential with a relative fast decay amplitude of ca. 77% (Fig. S9*A*). (*B*) Decreasing temperature increases t_{max}. Larger t_{max} at low temperature is a convoluted result of k_1, k_2 and k_{-1} (Eq. **S7**). Only mutants with observable intermediates at all three temperatures are shown. (*C*) Larger ratio of $t_{1/2}$ for OD_{330} over that in the NMR A signal as temperature decreases. $T119M^F$ is not shown since it is aggregation-resistant at 277 K for at least two weeks.

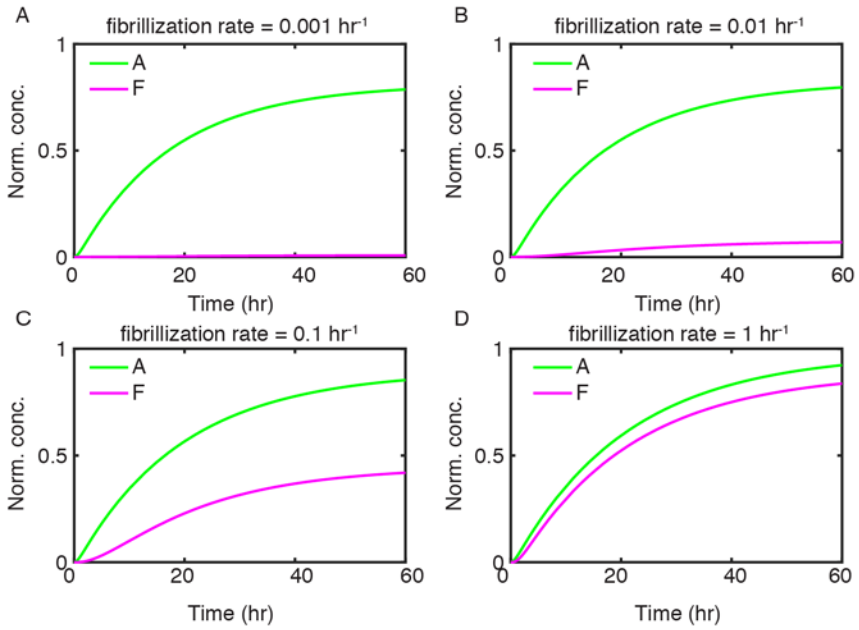

Fig. S7. Numerical simulations show that the lag time between the missing amplitude in the NMR signal (A signal) and the OD signal (associated with fibrils and other amorphous aggregates) decreases as the fibrillization rate increases from (*A*) to (*D*), analogous to the effects of increasing temperature in ^{19}F-NMR and OD experiments. The kinetics scheme is a three-step reversible scheme: $\mathrm{T} \underset{k_{-1}}{\overset{k_1}{\rightleftharpoons}} \mathrm{I} \underset{k_{-2}}{\overset{k_2}{\rightleftharpoons}} \mathrm{O} \underset{k_{-3}}{\overset{k_3}{\rightleftharpoons}} \mathrm{F}$, where O stands for small soluble oligomers and F represents fibrils and amorphous aggregates. The total concentration of T, I, O and F is normalized to unity. The concentrations of A (=O+F) and F are plotted in green and pink lines, respectively. For clarity, the curves for T and I are not shown. The fitted experimental parameters for TTR^F at 310 K are used in simulations as k_1, k_{-1}, k_2 and k_{-2}. The reverse fibrillization rate (k_{-3}) is set to 0.1 hr^{-1}. The forward fibrillization rate (k_3) is indicated at the top of each panel.

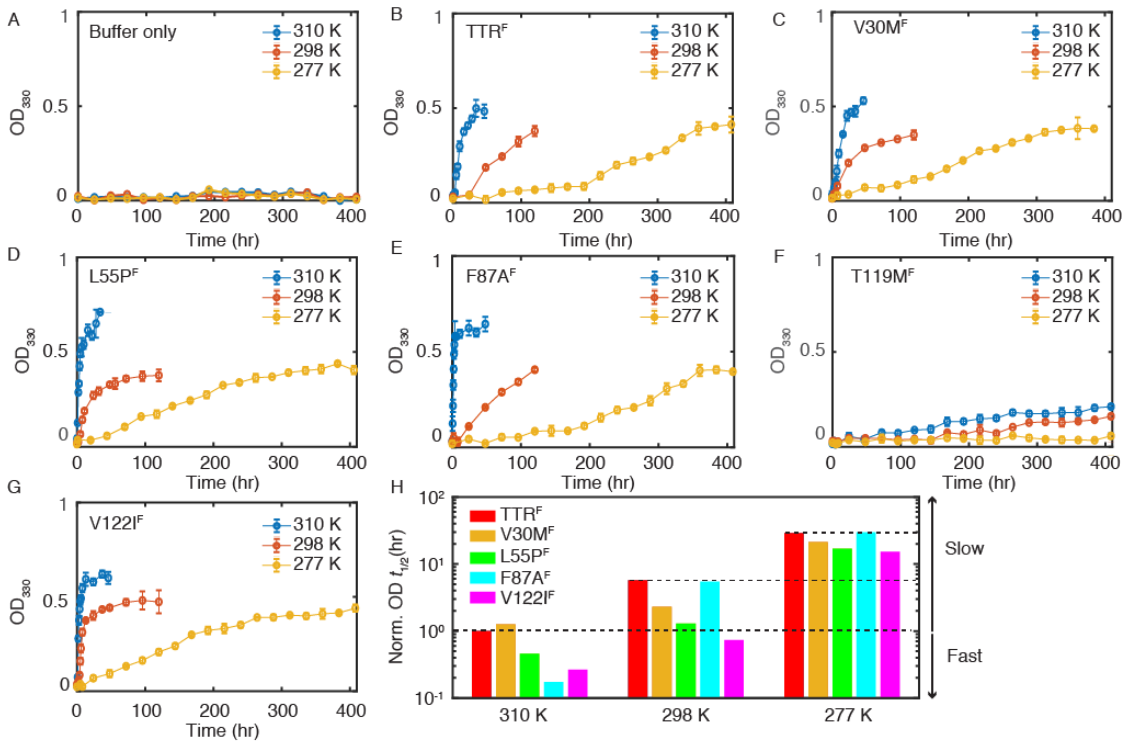

Fig. S8. Time dependent changes in turbidity (OD_{330}) for the buffer-only control (*A*) and various TTR mutants at pH 4.4 (*B*–*G*) and 310 K (blue), 298 K (red) and 277 K (orange). Data for TTR^F (*B*) are reproduced from Figs. S2*B*–*D* for easy comparison. The construct name is denoted at the top of each panel. Solid connecting lines are for eye guidance. Error bars represent one standard deviation from three independent measurements. (*H*) The OD $t_{1/2}$ as a function of mutation and temperature. These data are normalized using the OD $t_{1/2}$ of TTR^F at 310 K as reference. Note that the log y axis is used to show the vastly different OD $t_{1/2}$ at 310 K and 277 K in the same plot. The dashed line denotes no changes compared to the TTR^F data at each temperature. Note that all pathogenic mutants aggregate faster than TTR^F at all three temperatures (i.e., smaller OD $t_{1/2}$), except for $V30M^F$ at 310 K. $F87A^F$ aggregates faster than TTR^F at 310 K and similarly as TTR^F at 298 K and 277 K.

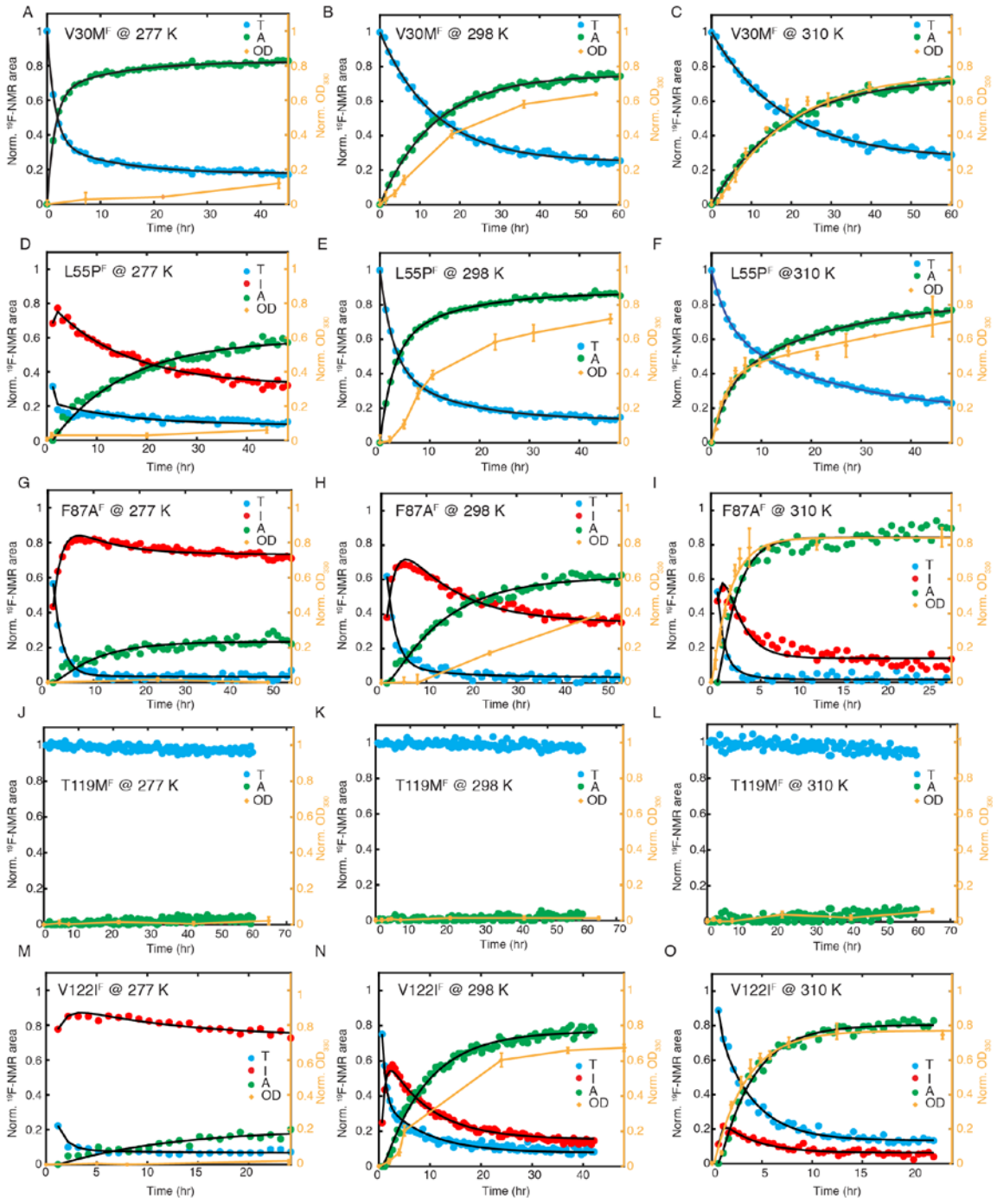

Fig. S9. Comparison of ^{19}F-NMR and turbidity for characterizing the aggregation kinetics of various TTR mutants as a function of temperature. The axis for normalized NMR data is on the left (black) and the one for OD_{330} is on the right (orange). The maximal OD_{330} is normalized to the maximum of A signal for easy viewing. (*A–C*) $V30M^F$ at 277 K, 298 K and 310 K. (*D–F*) $L55P^F$ at 277 K, 298 K and 310 K. (*G–I*) $F87A^F$ at 277 K, 298 K and 310 K. (*J–L*) $T119M^F$ at 277K, 298 K and 310 K. (*M–O*) $V122I^F$ at 277 K, 298 K and 310 K. In the presence of intermediate(s) (I, red), the two-step reversible kinetics scheme

(Scheme 1) was used to fit the NMR data (*D*, *G*, *H*, *I*, *M*, *N* and *O*). The following NMR fits apply to the cases where aggregation occurs without quantifiable intermediates (*A*–*C*, *E*–*F*): The decrease in $V30M^F$ tetramer signal at 298 K and 310 K (*B* and *C*) was fitted to a single exponential function, which does not exclude a multi-step mechanism; for the data at 277 K (*A*) fitted better to a double exponential (adjusted R^2 = 0.990) than a single exponential (adjusted R^2 = 0.951); for $L55P^F$, a double exponential function fitted the tetramer data at 298 K (adjusted R^2 = 0.998) (*E*) and 310 K (adjusted R^2 = 0.996) (*F*) better than a single exponential function (adjusted R^2 = 0.981 at 298 K and 0.982 at 310 K, respectively). No fitting was performed for the NMR and OD_{330} data for $T119M^F$ in this figure since no aggregation occurred within 60 hours. For the rest of the variants, only the OD_{330} data at 310 K was fitted due to the small lag time (< 1 hr) relative to the overall aggregation over ca. 2 days (also see the simulation justification in *SI text*): The OD data at 310 K for $V30M^F$ (*C*), $F87A^F$ (*I*) and $V122I^F$ (*O*) were approximated using a single exponential function; the OD_{330} data for $L55P^F$ at 310 K (*F*) were approximated using a double exponential function which fitted better (adjusted R^2 = 0.975) than a single exponential function (adjusted R^2 = 0.920). The orange connecting lines of OD_{330} data at 277 K and 298 K are to facilitate viewing only. NMR fits are in shown as black lines and OD_{330} fits at 310 K as orange lines. In all cases at 310 K (*C*, *F*, *I*, *L* and *O*), good agreement between the A signal (green) and the OD_{330} signal (orange) is evident (see Fig. S5*C*).

References

1. Sun X, Dyson HJ, & Wright PE (2017) Fluorotryptophan incorporation modulates the structure and stability of transthyretin in a site-specific manner. *Biochemistry* 56(41):5570–5581.
2. Hurshman AR, White JT, Powers ET, & Kelly JW (2004) Transthyretin aggregation under partially denaturing conditions is a downhill polymerization. *Biochemistry* 43(23):7365–7381.
3. Cantor CR & Schimmel PR (1980) *Biophysical Chemistry: Part III: The Behavior of Biological Macromolecules* (W. H. Freeman).
4. Luo LS, Burkart MD, Stachelhaus T, & Walsh CT (2001) Substrate recognition and selection by the initiation module PheATE of gramicidin S synthetase. *J Am Chem Soc* 123(45):11208–11218.
5. Luo LS & Walsh CT (2001) Kinetic analysis of three activated phenylalanyl intermediates generated by the initiation module PheATE of gramicidin S synthetase. *Biochemistry* 40(18):5329–5337.
6. Ditchfield R, Hehre WJ, & Pople JA (1971) Self-consistent molecular-orbital methods .9. Extended Gaussian-type basis for molecular-orbital studies of organic molecules. *J Chem Phys* 54(2):724.
7. Jakalian A, Bush BL, Jack DB, & Bayly CI (2000) Fast, efficient generation of high-quality atomic charges. AM1-BCC model: I. Method. *J Comput Chem* 21(2):132–146.
8. Peterson SA, *et al.* (1998) Inhibiting transthyretin conformational changes that lead to amyloid fibril formation. *Proc Natl Acad Sci USA* 95(22):12956–12960.
9. Case DA, *et al.* (2017) AMBER 2016. (University of California, San Francisco).
10. Maier JA, *et al.* (2015) ff14SB: Improving the accuracy of protein side chain and backbone parameters from ff99SB. *J Chem Theory Comput* 11(8):3696–3713.
11. Schrödinger, LLC (2017) The PyMOL molecular graphics system, version 1.8.2.3.
12. Rappley I, *et al.* (2014) Quantification of transthyretin kinetic stability in human plasma using subunit exchange. *Biochemistry* 53(12):1993–2006.
13. Schneider F, Hammarstrom P, & Kelly JW (2001) Transthyretin slowly exchanges subunits under physiological conditions: A convenient chromatographic method to study subunit exchange in oligomeric proteins. *Protein Sci* 10(8):1606–1613.
14. Hammarstrom P, Jiang X, Hurshman AR, Powers ET, & Kelly JW (2002) Sequence-dependent denaturation energetics: A major determinant in amyloid disease diversity. *Proc Natl Acad Sci USA* 99 Suppl 4:16427–16432.